Capillarity

Vol. 18, No. 2, p. 41-49, 2026

Original article

Simulations of inertial liquid-lens coalescence with the pseudopotential lattice Boltzmann method

Qingguang Xie[1]*, Jens Harting[1,2]

[1]*Helmholtz Institute Erlangen-Nürnberg for Renewable Energy (IET-2), Forschungszentrum Jülich, Erlangen 91058, Germany*

[2]*Department of Chemical and Biological Engineering and Department of Physics, Friedrich-Alexander-Universität Erlangen-Nürnberg, Erlangen 91058, Germany*

Keywords:
Coalescence
liquid lenses
lattice Boltzmann method

Cited as:
Xie, Q., Harting, J. Simulations of inertial liquid-lens coalescence with the pseudopotential lattice Boltzmann method. Capillarity, 2026, 18(2): 41-49.
https://doi.org/10.46690/capi.2026.02.01

Abstract:
The coalescence of liquid lenses is relevant in various applications, including inkjet printing and fog harvesting. However, the dynamics of liquid-lens coalescence have been relatively underexplored, particularly in the case of liquid lenses with larger contact angles. The coalescence of low-viscosity liquid lenses is numerically investigated by means of the pseudopotential multi-component lattice Boltzmann method over a wide range of contact angles. In two-dimensional simulations, numerical results on the growth of the bridge height are in quantitative agreement with experimental measurements for small contact angles. In addition, a comparison of the simulation results with a theoretical approach based on the thin-sheet equations for liquid lenses shows that these equations accurately capture the bridge-growth dynamics up to moderate contact angles. For the three-dimensional case, the growth of the bridge radius is independent of the equilibrium contact angle of the liquid lenses at the initial stage of growth. The dependency between the growth of the bridge height and the bridge radius exhibits a non-linear to linear transition.

1. Introduction

The coalescence of droplets is a fundamental process relevant to natural phenomena and many industrial applications, such as formation of rain drops (Low and List, 1982), stability of emulsions (Kumar et al., 1996; Goff, 1997), enhanced oil recovery (Perazzo et al., 2018), coating (Eslamian and Soltani-Kordshuli, 2018) and printing (Wijshoff, 2018). Coalescence is initiated when two droplets come into contact and form a growing liquid bridge. Finally, the two droplets merge into a single droplet, which relaxes to its equilibrium shape. The growth of the bridge is controlled by the interplay of capillarity, viscosity and inertia, and exhibits three different dynamic regimes: the inertial limited viscous regime (Paulsen et al., 2012; Paulsen, 2013; Anthony et al., 2020), the viscous regime (Hopper, 1984, 1990; Eggers et al., 1999), and the inertial regime (Aarts et al., 2005; Paulsen et al., 2011). These regimes are typically characterized by the Ohnesorge number, $Oh = \eta/\sqrt{\rho R\gamma}$, where η is the dynamic viscosity of the droplet liquid, ρ is the droplet liquid density, R is the droplet radius, and γ is the surface tension of the droplet. This dimensionless number measures the dominance of viscosity over inertia. For $Oh \gg 1$, coalescence occurs in the viscous regime, whereas $Oh \ll 1$ indicates the inertial regime. The corresponding characteristic timescales are the viscous time, $\tau_v = \eta R/\gamma$, and the inertial time, $\tau_i = \sqrt{\rho R^3/\gamma}$ (Eggers et al., 2025). The coalescence of suspended droplets in a fluid phase (Eggers et al., 1999; Duchemin et al., 2003; Aarts et al., 2005; Thoroddsen et al., 2007) and sessile droplets on a substrate (Ristenpart et al., 2006; Narhe et al., 2008; Hernández-Sánchez et al., 2012; Lee et al., 2012) have been

Yandy Scientific Press

*Corresponding author.
E-mail address: q.xie@fz-juelich.de (Q. Xie); j.harting@fz-juelich.de (J. Harting).

Received November 16, 2025; revised December 13, 2025; accepted January 2, 2026; available online January 5, 2026.

investigated extensively. At the initial stage of coalescence, in the viscous regime, the radius of the bridge grows as $r_0 \sim t$ for both spherical droplets and sessile droplets (Hernández-Sánchez et al., 2012), whereas, in the inertial regime, the radius of bridge grows following $r_0 \sim t^{1/2}$ for spherical droplets (Burton and Taborek, 2007; Paulsen et al., 2011; Xia et al., 2019) and $r_0 \sim t^{2/3}$ for sessile droplets on a substrate (Eddi et al., 2013), which indicates that the geometry of droplets has a strong effect on the coalescence dynamics. The crossover from the viscous regime to the inertial regime of the bridge growth for spherical drops depends on fluid properties and drop size (Paulsen et al., 2011; Xia et al., 2019).

However, the coalescence of liquid lenses at a liquid layer has been less investigated (Eggers et al., 2025), despite its significance in applications such as water harvesting, wet-on-wet printing and droplets on a lubricated surface. Burton and Taborek (2007) found that the bridge radius r_0 of coalescing dodecane lenses at a water-air interface grows following a $t^{1/2}$ scaling law in the inertial regime, surprisingly the same as that of suspended droplets. Recently, Hack et al. (2020) investigated the coalescence of dodecane lenses at a water-air interface experimentally and applied a theoretical approach based on the thin-sheet equations to describe the growth of the bridge height. They found that the growth of the vertical bridge height h_0 follows a $h_0 \sim t$ scaling in the viscous regime and a $h_0 \sim t^{2/3}$ scaling in the inertial regime, which agrees with the theoretical prediction. Very recently, Scheel et al. (2023) performed color-gradient lattice Boltzmann simulations of the coalescence of liquid lenses over a wide range of surface tension and viscosity values, successfully capturing the asymptotic temporal behavior in both the viscous and inertial limits. Furthermore, Padhan and Pandit (2023) applied a three-phase Cahn-Hilliard-Navier-Stokes approach to study the spatiotemporal evolution of the fluid velocity, vorticity, and the concentration fields in liquid-lens coalescence. The above experimental and numerical studies are primarily limited to liquid lenses with small contact angles and only address the initial stage of coalescence, leaving the coalescence of liquid lenses with large contact angles and the coalescence dynamics at later stages largely unexplored.

Here, the coalescence of two low-viscosity liquid lenses at a liquid-liquid interface is numerically investigated. The pseudopotential multi-component lattice Boltzmann method is applied to simulate the fluid phases in two-dimensional (2D) and three-dimensional (3D). The pseudopotential multi-component lattice Boltzmann method (LBM) may offer a significant reduction in computational cost and a simpler implementation compared to both the color-gradient lattice Boltzmann and Cahn-Hilliard-Navier-Stokes approaches, but leaves less flexibility in, for example, the choice of surface tensions.

The investigation focuses on the impact of contact angles on the initial coalescence dynamics of liquid lenses, comparing simulation results with experimental findings and theoretical analysis based on the thin-sheet equations. In the 2D simulations, results agree quantitatively with experimental results and theoretical analysis for small contact angles, $\theta < 40^\circ$, while at large contact angles, the theoretical model based on the thin-sheet equations overestimates the bridge growth. For the 3D cases, it is found that that during coalescence, the cross-section of the bridge is of a spherical cap shape; however, the contact angle of the cross-section is less than the equilibrium contact angle at the initial state, which reveals a non-linear dependence of the growth of the bridge radius and the bridge height at the initial stage.

2. Method

The LBM is applied to simulate the dynamics of fluids. In the past decades, the LBM has been used as a powerful tool for numerical simulations of fluid flows (Succi, 2001; Krüger et al., 2017) and has been extended to simulate multi-phase/multicomponent fluids (Shan and Chen, 1993; Cappelli et al., 2015). Moreover, the LBM has been applied successfully to investigate viscous and inertial coalescence of suspended droplets (Gross et al., 2013; Lim et al., 2017) and sessile droplets on a substrate (Hessling, 2017). The pseudopotential multicomponent LBM of Shan and Chen (1993, 1994) with a D3Q19 lattice (Qian et al., 1992) is utilized, and related details are reviewed in the following. Three fluid components follow the discretized equation of each distribution function according to the lattice Boltzmann equation:

$$f_i^c(\vec{x}+\vec{e}_i\Delta t, t+\Delta t) = f_i^c(\vec{x},t) + \Omega_i^c(\vec{x},t) \tag{1}$$

where $i = 1, \ldots, 19$. $f_i^c(\vec{x},t)$ are the single-particle distribution functions for fluid component $c = 1$, 2 or 3, $\vec{e}_i$ is the discrete velocity in the i-th direction, and:

$$\Omega_i^c(\vec{x},t) = -\frac{f_i^c(\vec{x},t) - f_i^{\mathrm{eq}}(\rho^c(\vec{x},t), \vec{u}^c(\vec{x},t))}{\tau^c}\Delta t \tag{2}$$

is the Bhatnagar-Gross-Krook collision operator (Bhatnagar et al., 1954). τ^c is the relaxation time for component c. Here, $f_i^{\mathrm{eq}}(\rho^c(\vec{x},t), \vec{u}^c(\vec{x},t))$ is a second-order equilibrium distribution function (Chen et al., 1992), defined as:

$$f_i^{\mathrm{eq}}(\rho^c, \mathbf{u}^c) = \omega_i \rho^c \left[1 + \frac{\mathbf{e}_i \cdot \mathbf{u}^c}{c_s^2} - \frac{(\mathbf{u}^c \cdot \mathbf{u}^c)}{2c_s^2} + \frac{(\mathbf{e}_i \cdot \mathbf{u}^c)^2}{2c_s^4}\right] \tag{3}$$

where ω_i is a coefficient depending on the direction: $\omega_0 = 1/3$ for the zero velocity, $\omega_{1,\ldots,6} = 1/18$ for the six nearest neighbors and $\omega_{7,\ldots,18} = 1/36$ for the nearest neighbors in diagonal direction. $c_s = \Delta x/(\sqrt{3}\Delta t)$ is the speed of sound. The macroscopic variables, densities and velocities are updated as $\rho^c(\vec{x},t) = \rho_0 \sum_i f_i^c(\vec{x},t)$, where ρ_0 is a reference density, and $\vec{u}^c(\vec{x},t) = \sum_i f_i^c(\vec{x},t)\vec{c}_i/\rho^c(\vec{x},t)$, respectively. The single relaxation time scheme is employed in this work. While the multi-relaxation time scheme (Fan, 2010) can enhance stability for high Reynolds number or low-viscosity flows, it incurs a higher computational cost due to the required moment-space transformations. Given the low Reynolds numbers and moderate viscosities considered here, single relaxation time provides a stable and computationally efficient alternative.

LBM can be treated as an alternative solver of Navier-Stokes equation in the limit of small Knnudsen and Mach numbers (Succi, 2001). In the simulations, the lattice constant Δx, the timestep Δt, the reference density ρ_0, and the relaxation time τ^c are chosen to be unity, which results in a kinematic viscosity $\nu^c = 1/6$ in lattice units.

In the pseudopotential multicomponent LBM introduced by Shan and Chen (1993), a mean-field interaction force between fluid components c and c' is introduced, written as:

$$\vec{F}_{\mathrm{C}}^{c}(\vec{x},t) = -\Psi^{c}(\vec{x},t)\sum_{c'} g_{cc'}\sum_{\vec{x}'}\Psi^{c'}(\vec{x}',t)(\vec{x}'-\vec{x}) \tag{4}$$

in which $\vec{x}'$ denote the nearest neighbours of lattice site $\vec{x}$ and $g_{cc'}$ is a coupling constant determining the surface tension. $\Psi^{c}(\mathbf{x},t)$ is called "effective mass", defined as (Shan and Chen, 1993, 1994):

$$\Psi^{c}(\vec{x},t) \equiv \Psi(\rho^{c}(\vec{x},t)) = 1 - e^{-\rho^{c}(\vec{x},t)} \tag{5}$$

This effective mass formulation ensures that at low densities it approximates the density ρ^{c} itself, while at high densities it asymptotically approaches a saturation limit (Chen et al., 2014). The saturation behavior prevents the collapse of the high-density phase, thereby enhancing numerical stability in simulations.

The force $\vec{F}_{\mathrm{C}}^{c}(\vec{x},t)$ is then incorporated into the lattice Boltzmann equations by adding a shift $\Delta\vec{u}^{c}(\vec{x},t) = \tau^{c}\vec{F}_{\mathrm{C}}^{c}(\vec{x},t)/\rho^{c}(\vec{x},t)$ to the velocity $\vec{u}^{c}(\vec{x},t)$ in the equilibrium distribution function f_{i}^{eq}. The pseudopotential multicomponent LBM is a diffuse interface method with an interface width of $\approx 5\Delta x$, which elegantly removes the stress singularity at the moving contact line usually occurring in sharp-interface models. It is noted that in the pseudopotential LBM, the surface tension is governed by the interaction parameter $g_{cc'}$ in Eq. (4) and is calculated by the Young-Laplace equation. For a spherical droplet of radius R immersed in another fluid, the Young-Laplace equation, $\gamma = R\Delta P/2$, relates the pressure difference ΔP over the interface between two fluids to the surface tension γ.

Simulations are performed in 2D and 3D. For simplicity and numerical stability, the three fluid components are initialized with equal viscosity and density.

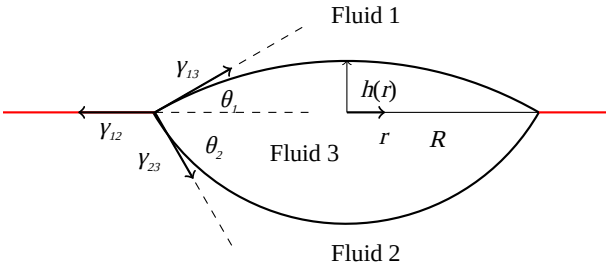

Fig. 1. Schematic of a single liquid lens (fluid 3) at an interface between fluid 1 and fluid 2 in the equilibrium state.

3. Results and discussion

3.1 Single liquid lens

The study begins with the spreading of a single liquid lens at a fluid-fluid interface to validate its equilibrium shape, as illustrated in Fig. 1. γ_{ij} is the surface tension at the interface between fluid i and fluid j (i, j = 1, 2, 3). The base radius of the lens is R, and the lens height is $h(r)$ along the radial coordinate. The contact angles of the upper and lower parts of the lens are θ_1 and θ_2, respectively. The equilibrium shape of a liquid lens has been investigated theoretically and experimentally, and has been used as a classical benchmark problem to test the numerical approaches for three-phase flows (Burton et al., 2010; Zheng and Zheng, 2019; Yuan et al., 2020; Ravazzoli et al., 2020).

When a spherical droplet is initially located at a fluid-fluid interface, it undergoes deformation driven by surface tension to reach its equilibrium state. In the case where gravity is negligible, the liquid lens assumes a spherical cap shape, dominated by surface tension. At the three-phase contact line, the surface tensions obey the so-called Neumann's law $\vec{\gamma}_{12}+\vec{\gamma}_{13}+\vec{\gamma}_{23}=0$ and after some mathematical manipulations, the following is obtained:

$$\cos\theta_1 = \frac{\gamma_{13}^2-\gamma_{23}^2+\gamma_{12}^2}{2\gamma_{12}\gamma_{13}}, \quad \cos\theta_2 = \frac{\gamma_{23}^2-\gamma_{13}^2+\gamma_{12}^2}{2\gamma_{12}\gamma_{23}} \tag{6}$$

where $\gamma_{ij} = |\vec{\gamma}_{ij}|$. The height profiles of the upper and lower parts of the lens along the radial coordinate follow:

$$h_{up}(r) = \sqrt{\left(\frac{R}{\sin\theta_1}\right)^2 - r^2} - R\cot\theta_1 \tag{7}$$

$$h_{lo}(r) = \sqrt{\left(\frac{R}{\sin\theta_2}\right)^2 - r^2} - R\cot\theta_2 \tag{8}$$

The simulations utilize a 2D system of size 512×264. A wall is placed at the bottom of the system, and periodic boundary conditions are applied at the remaining boundaries. A spherical droplet of radius $R_0 = 80$ is initialized at the center of a fluid-fluid interface and allowed to equilibrate. The densities of the three fluids are set to $\rho_i = 0.7$. The surface tension ratios are varied to $\gamma_{12}:\gamma_{13}:\gamma_{23} = 1:1:1$, $\gamma_{12}:\gamma_{13}:\gamma_{23} = 1.5:1:1$ and $\gamma_{12}:\gamma_{13}:\gamma_{23} = 1:1.5:1$. In the case of $\gamma_{12}:\gamma_{13}:\gamma_{23} = 1:1:1$, the contact angles are $\theta_1 = \theta_2 \sim 60^\circ$, as shown in Fig. 2(a). For $\gamma_{12}:\gamma_{13}:\gamma_{23} = 1.5:1:1$, the lens spreads more at the fluid interface to reduce the total surface

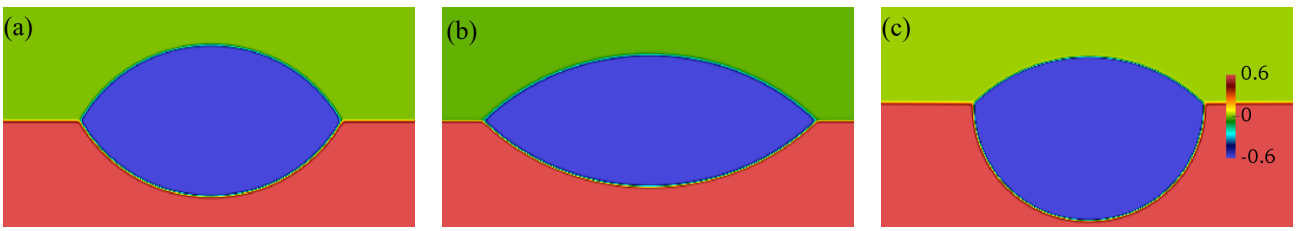

Fig. 2. Snapshots of a single liquid lens in equilibrium state obtained in simulations for different combinations of surface tensions: (a) $\gamma_{12}:\gamma_{13}:\gamma_{23} = 1:1:1$, (b) $\gamma_{12}:\gamma_{13}:\gamma_{23} = 1.5:1:1$, and (c) $\gamma_{12}:\gamma_{13}:\gamma_{23} = 1:1.5:1$.

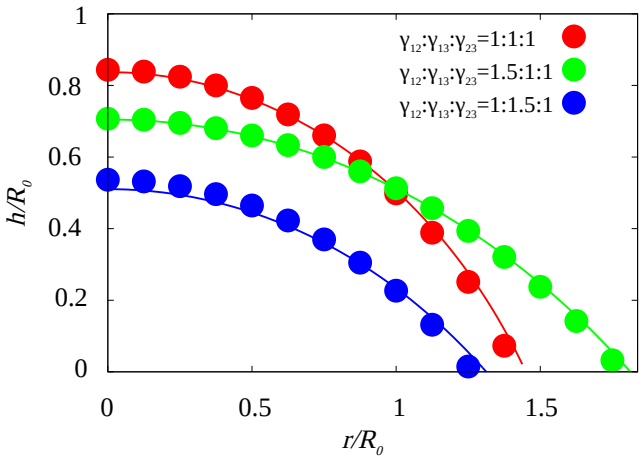

Fig. 3. The height profile of the upper half of a single liquid lens in equilibrium state for different surface tension ratios.

energy (Fig. 2(b)), resulting in lower contact angles $\theta_1 = \theta_2 \sim 42°$. When $\gamma_{12} : \gamma_{13} : \gamma_{23} = 1 : 1.5 : 1$, to minimize the total surface energy, the lens sinks more in the lower fluid (Fig. 2(c)) and the contact angles are $\theta_1 \sim 42°$ and $\theta_2 \sim 97°$. After equilibrium, the height of the liquid lens is measured as a function of the radial coordinate. The simulation results are then compared with the analytical solution Eq. (7) in Fig. 3. Determining the exact position of the diffuse interface is challenging; here, the interface position is defined as corresponding to zero density difference between the lens liquid and the surrounding liquid, e.g., $\rho^2 - \rho^3 = 0$. The simulation results agree quantitatively with the analytical solution Eq. (7), which demonstrates that the LBM can accurately capture the equilibrium interface shape of a single liquid lens.

3.2 Two liquid lenses-2D

Here, the coalescence dynamics of liquid lenses at a fluid-fluid interface are considered, as illustrated in Fig. 4. The lenses are up-down symmetric, and the contact angles are $\theta_1 = \theta_2 = \theta$. The maximal bridge height is H, and the bridge height at the center is h_0. L is the distance between the far ends of the two lenses. For the coalescence of liquid lenses, the crossover length scale and time scale from the viscous to the inertial regime are determined as (Hack et al., 2020) $h_c \sim \eta^2/(\rho\gamma^2)$ and $t_c \sim \eta^3/(\rho\gamma^2\theta^2)$, where η is the dynamic viscosity of lens liquid, and γ is the surface tension of the lens with respect to its surrounding fluids. Using the parameters in the simulations, $h_c \sim 0.4$ lattice units and $t_c \sim 2$ timesteps are obtained, indicating that all simulations are in the inertial regime. For liquid lenses with small contact angles, assuming the flow inside the lenses is dominant and parallel to the vertical plane, the dynamics at the initial stage of coalescence are described by 2D thin-sheet equations (Erneux and Davis, 1993; Scheid et al., 2012; Eggers and Fontelos, 2015; Hack et al., 2020), written as:

$$h_t + (uh)_x = 0, \quad \rho(u_t + uu_x) = \gamma h_{xxx} + 4\eta\frac{(u_x h)_x}{h} \tag{9}$$

which represent mass conservation and momentum conservation, respectively. Here, $h(x,t)$ describes the shape of the bridge and $u(x,t)$ is the horizontal velocity of liquid inside the lens. The lower indices denote spatial and temporal derivatives.

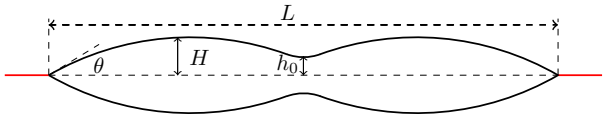

Fig. 4. Schematic of the side view of two coalescing lenses at a fluid-fluid interface. The lenses are up-down symmetric, and the contact angle is θ. The maximal bridge height is H, and the bridge height at the center is h_0. L is the distance between the far ends of the two lenses.

When inertia dominates over viscosity, the above thin-sheet equations are simplified in the inviscid limit to (Hack et al., 2020):

$$h_t + (uh)_x = 0, \quad \rho(u_t + uu_x) = \gamma h_{xxx} \tag{10}$$

Hack et al. (2020) found experimentally that the bridge growth of two equally sized liquid lenses shows a self-similar dynamics, which motivated them to solve Eq. (10) by introducing similarity solutions written as:

$$h(x,t) = kt^{\alpha}\mathscr{H}(\xi), \quad u(x,t) = \frac{\alpha k}{\theta}t^{\beta}\mathscr{U}(\xi) \tag{11}$$

where $\mathscr{H}$ and $\mathscr{U}$ are the similarity functions for the bridge profile and horizontal velocity inside the lenses, and k is a parameter dependent on surface tension, contact angle and density. The parameter $\xi = \theta x/(kt^{\alpha})$ is chosen to ensure that $h(x,t) \simeq \theta x$ far away from the bridge. By inserting Eq. (11) into Eq. (10), they obtained $\alpha = 2/3$, $\beta = -1/3$. By satisfying certain boundary conditions, the time evolution of the bridge height is written as (Hack et al., 2020):

$$h_0 = kt^{2/3} = \left(\frac{9K_i\gamma\theta^4}{2\rho}\right)^{1/3} t^{2/3} \tag{12}$$

in which $K_i = 0.106$ is obtained by numerically solving the boundary value problem. The bridge profile and horizontal velocity profile can be written as (Hack et al., 2020):

$$h(x,t) = h_0\mathscr{H}(\xi), \quad u(x,t) = \frac{2h_0}{3\theta t}\mathscr{U}(\xi) \tag{13}$$

Simulations of liquid lens coalescence in 2D are conducted. To capture the initial stage of coalescence where the bridge growth is not affected by the finite height of the lens, a sufficiently large initial height of the lens is required. A spherical cap-shaped lens is initialized at the fluid interface with maximal height $H = 1,000$ and contact angles $\theta = 22°$, $35°$, $59°$, respectively. It is noted that the contact angles were measured after the initially configured single-droplet lens had relaxed to equilibrium. After reaching equilibrium, the lens is numerically mirrored and located at a distance of ~ 2 lattice nodes from the original one.. It is noted that the initial distance between two lenses has no significant influence on coalescence dynamics (Hessling, 2017), and coalescence is predominantly driven by surface tensions. Given that the lenses approach with negligible relative velocity v, the associated Weber number $We = \rho v^2/(\gamma R)$ is much less than 1, which favors coalescence over phenomena like bouncing or breakup. The surface tension during coalescence remains constant, as the system is both

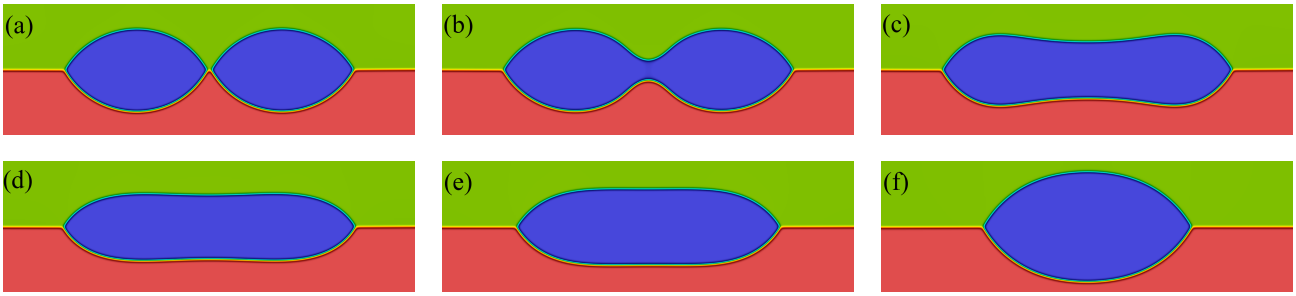

Fig. 5. Time sequence of the coalescence process of liquid lenses in a 2D system obtained in the simulations: (a) $t/T = 0$, (b) $t/T = 0.019$, (c) $t/T = 0.066$, (d) $t/T = 0.094$, (e) $t/T = 0.176$, and (f) $t/T = 1$.

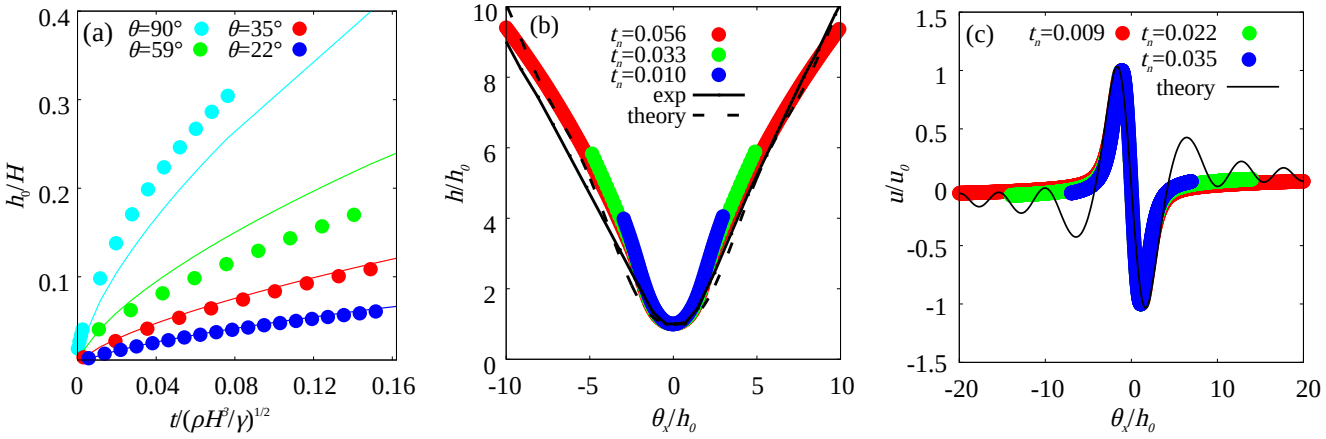

Fig. 6. (a) The time evolution of bridge height h_0 for different contact angles, (b) rescaled bridge profile for lenses with contact angle $\theta = 35°$ at different times $t_n = t/(\rho H^3/\gamma)^{1/2}$, and (c) rescaled horizontal velocity profile corresponds to different times $t_n = t/(\rho H^3/\gamma)^{1/2}$.

isothermal and free of surfactants.

The simulation captures the coalescence of two lenses, as illustrated in Fig. 5. The timestep is normalized by the total duration T, defined as the time from initial lens contact (Fig. 5(a)) to the formation of a single lens with a relaxed equilibrium shape (Fig. 5(f)). The color represents the density difference between the lens and the lower liquid. Upon contact (Fig. 5(a)), a fast-growing bridge is formed connecting the two lenses (Figs. 5(b) and 5(c)), while the distance L between the far ends of the two lenses remains almost constant. This indicates that at the initial stage of the coalescence, a strong velocity field is located near the bridge center, whereas the influence of coalescence at the far field is negligible. When the bridge height grows to be comparable to the maximal height H, the lens retracts (Figs. 5(c)-5(e)), and finally a single lens is formed at the interface which relaxes to its equilibrium shape (Fig. 5(f)).

The time evolution of the vertical height of the bridge center h_0 is shown in Fig. 6(a) for different contact angles. The bridge grows faster with increasing contact angle. For small contact angles $\theta < 40°$, the simulation results (symbols) agree quantitatively with the theoretical analysis Eq. (12) (solid lines). For a large contact angle $\theta = 59°$, the similarity solution based on the thin-sheet equations overestimates the bridge growth. The thin-sheet equations are based on the lubrication theory, which assumes that the film thickness (normal to the surface) is much smaller than the characteristic length scale along the surface. Consequently, these equations break down at large contact angles, where the interface height violates the underlying thin-film assumption. It is noted that the LBM method solves the Navier-Stokes equations and is valid for the whole range of contact angles. In the case of a contact angle of $\theta = 90°$, the coalescence of two suspended spherical droplets in another liquid is simulated. Interestingly, the theoretical prediction based on the thin-sheet equations underestimates the bridge growth-contrary to that at a contact angle of $\theta = 59°$.

The bridge profiles of coalescing liquid lenses are shown in Fig. 6(b) at a contact angle $\theta = 35°$ for different times $t_n = t/(\rho H^3/\gamma)^{1/2}$. The horizontal coordinate is rescaled by θ/h_0 and the vertical coordinate by h_0, respectively. All the bridge profiles collapse onto a universal curve, verifying the self-similar dynamics at the early stage of coalescence. The simulation results (symbols) agree quantitatively with experimental results (solid line) and theoretical analysis (dashed line) (Hack et al., 2020). It is noted that the simulation results slightly deviate from the experimental results at $\theta x/h_0 < -3$, possibly because the neighboring lenses are not of exactly equal size in experiments.

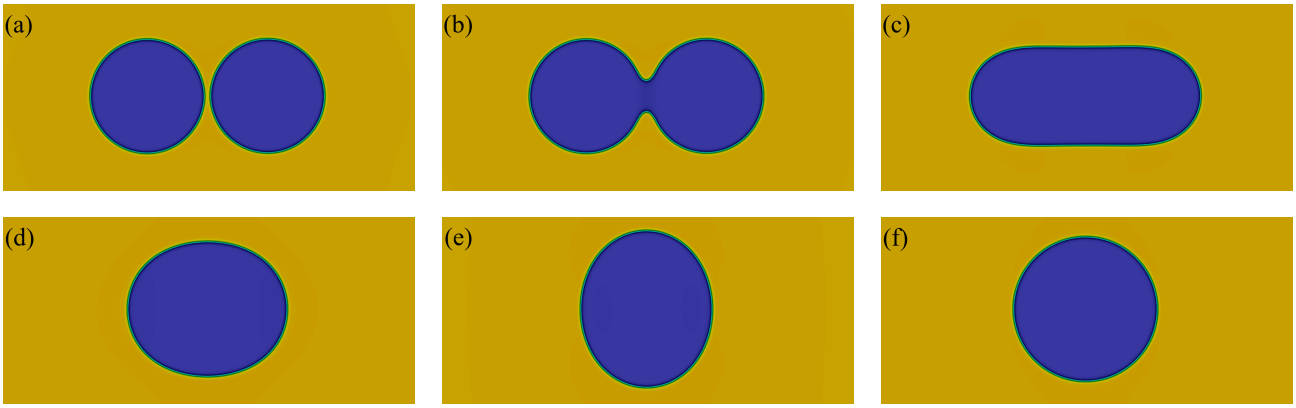

Fig. 7. Time sequence of the top-views of two coalescing lenses in 3D: (a) $t/T = 0$, (b) $t/T = 0.088$, (c) $t/T = 0.165$, (d) $t/T = 0.251$, (e) $t/T = 0.326$, and (f) $t/T = 1$.

Near the bridge center, the horizontal velocity profiles u are shown in Fig. 6(c) for different times $t_n = t/(\rho H^3/\gamma)^{1/2}$. The horizontal coordinate is rescaled with θ/h_0 and the vertical coordinate with the maximal horizontal velocity $u_0(t_n)$ at its corresponding time t_n. The velocity profiles u_x also collapse to a single curve, indicating self-similar dynamics. In contrast to the theoretical prediction Eq. (13) (solid line), the simulations do not exhibit strong oscillations of the horizontal velocity, which is likely due to the presence of viscous damping. In contrast, the theoretical analysis assumes an inviscid limit.

3.3 Two liquid lenses-3D

Here, simulations of liquid lens coalescence are carried out in three dimensions. The computational cost is extremely high for simulating lenses with an initial height $H \sim 1,000$. Therefore, to reduce computational cost, a spherical cap-shaped lens is initialized at the fluid interface with maximal height $H = 100$ and contact angles $\theta = 43°, 60°$, respectively. The system is allowed to equilibrate, after which it is mirrored and positioned next to the initial lens at a distance of approximately 2 lattice units. Fig. 7 shows the top-view of the coalescence process of two lenses obtained in the simulations. Similar to the side-views of the 2D simulations (Fig. 5), the bridge connecting two lenses grows fast initially (Figs. 7(a)-7(c)). At a later stage, the lens retracts (Figs. 7(c)-7(e)), followed by oscillations and finally relaxes to its equilibrium shape (Fig. 7(f)).

For contact angles of $\theta = 60°$ and $\theta = 43°$, the time evolution of the bridge height h_0 and radius r_0 is presented in Fig. 8(a). The vertical height of the bridge grows faster with a larger contact angle, similar to what was observed in the 2D simulations (see Fig. 6(a)). Interestingly, the horizontal radius of the bridge grows at the same speed for both contact angles in the initial stage, which indicates that the bridge radius growth is not affected by the initial contact angle of the lenses, and the growth of the bridge radius is not a linear function of the growth of bridge height, in contrast to that observed in coalescing sessile droplets on a substrate. A possible explanation is that due to the no-slip boundary condition, the coalescence speed of sessile droplets on a substrate is relatively slow, giving sufficient time for the cross-section of the bridge to relax immediately to a spherical cap shape with a corresponding equilibrium contact angle. However, the coalescence speed of liquid lenses at a fluid-fluid interface is significantly faster, and the bridge height and radius grow in a non-coupled manner, resulting in a non-linear dependence of bridge radius and height growth. Although the simulations were limited to contact angles of $\theta = 43°$ and $60°$ due to computational resource constraints, the initial growth of the bridge radius is expected to be independent of the contact angle across a wider range. This expectation is based on previous work, which shows that the growth of the width of coalescing lenses agrees with studies for freely suspended, respectively spherical droplets (Scheel et al., 2023). If one considers a horizontal cross-section through the liquid lenses, their coalescence resembles that of freely suspended droplets with an effective contact angle of $90°$. In this view, the contact angle observed in the vertical cross-section plays a negligible role in the initial stage.

Next, the shape of the cross-section of the bridge is explored. Fig. 8(b) depicts the upper quarter of the lens for different times t_n obtained in the simulations (symbols). The shape of the cross-section of the bridge can be accurately described by a spherical cap (solid lines), dominated by surface tensions. However, the contact angles of the cross-section obtained by fitting the shape with a spherical cap function vary over time. Fig. 8(c) shows the time evolution of the contact angle θ_c of the cross section of the bridge. The contact angle θ_c is less than the equilibrium contact angle θ_{eq} and increases rapidly in the initial stage, which indicates that the bridge radius grows faster than the bridge height.The contact angle reaches a plateau at the intermediate stage, demonstrating a linear relation of the growth of bridge height and bridge width, $r_0/h_0 = \cos\theta_c/(1-\sin\theta_c)$. Afterwards, due to oscillation of the lens, the contact angle decreases, followed by an increase. Finally, the contact angle θ_c of the cross-section of the bridge arrives at the equilibrium contact angle.

4. Conclusion

The inertial coalescence of liquid lenses over a wide range of contact angles is numerically investigated using the

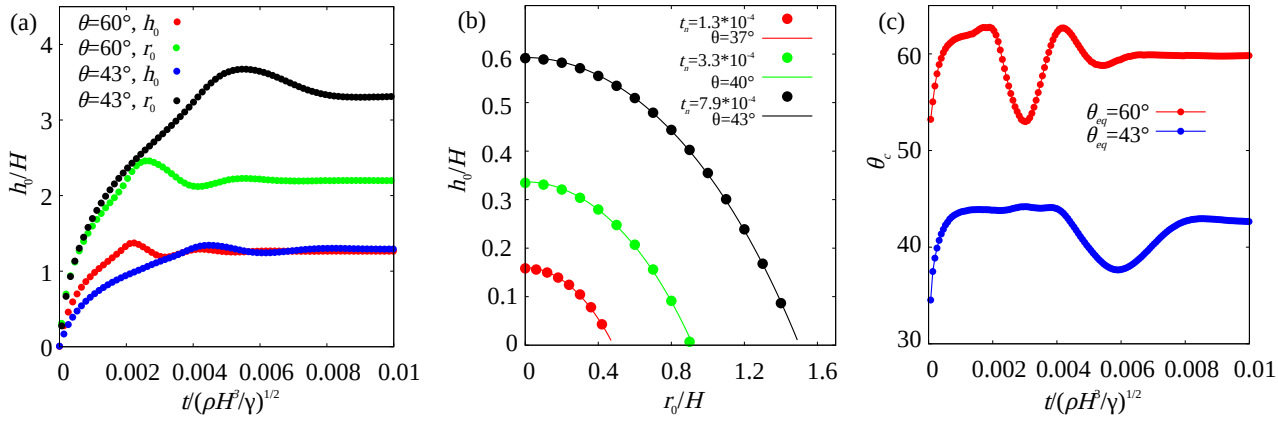

Fig. 8. (a) the time evolution of bridge height h_0 and radius r_0 for different contact angles, (b) the shape of the cross-section of the bridge at different times, and (c) the time evolution of contact angle θ_c of the bridge cross section.

pseudopotential LBM. While prior work has focused largely on liquid lenses with small contact angles and only addresses the initial stage of coalescence, this work extends the analysis to the coalescence of liquid lenses with large contact angles and the coalescence dynamics at later stages.

The simulations in 2D successfully capture the self-similar dynamics of both the bridge and velocity profiles, showing quantitative agreement with experimental observations and a theoretical framework based on thin-sheet equations. Furthermore, the simulation results demonstrate that the thin-sheet equations are applicable to describe the quantitative behavior of bridge growth for small contact angles approximately up to $\theta < 40^\circ$. In the 3D case, the bridge height is found to grow faster with a larger contact angle, while the growth of the bridge radius is independent of the contact angle at the initial stage. The contact angle of the cross-section of the bridge increases rapidly in the initial stage. It reaches a plateau at the intermediate stage, indicating a transition from a non-linear to a linear dependency between the growth of bridge height and bridge width. A theoretical model capable of predicting the transition's critical conditions, such as the critical bridge radius or time, and describing the full bridge growth dynamics is not yet available. Developing such a model extends beyond the scope of the current work and represents a valuable direction for future research.

The pseudopotential LBM has been widely applied to study binary fluid component systems (Liu et al., 2016; Krüger et al., 2017; Xie et al., 2025), and the result demonstrate its applicability to ternary fluid systems, potentially inspiring its use for investigating printing and coating multi-component solutions for functional material synthesis in catalytic and electronic applications (Steinberger et al., 2024; Vinodh et al., 2024). For instance, in wet-on-wet inkjet printing, the final deposition pattern is affected by the competition between coalescence and evaporation timescales (Wijshoff, 2018). Our findings provide an estimate of the coalescence timescale, thereby offering practical guidelines for optimizing drying conditions.

Acknowledgements

Fruitful discussions with Jacco Snoeijer, Michiel Hack, and Walter Tewes are gratefully acknowledged. Financial support is acknowledged from the Deutsche Forschungsgemeinschaft (DFG, German Research Foundation) Project-ID 431791331 (CRC1452 CLINT), and the German Federal Ministry of Education and Research (BMBF)–Project H2Giga/AEM-Direkt (Grant number 03HY103HF). The Gauss Centre for Supercomputing e.V. (www.gauss-centre.eu) is thanked for funding this project by providing computing time through the John von Neumann Institute for Computing (NIC) on the GCS Supercomputer JUWELS at Jülich Supercomputing Centre (JSC).

Conflicts of interest

The authors declare no competing interest.

References

Aarts, D. G. A. L., Lekkerkerker, H. N. W., Guo, H., et al. Hydrodynamics of droplet coalescence. Physical Review Letters, 2005, 95(16): 164503.

Anthony, C. R., Harris, M. T., Basaran, O. A. Initial regime of drop coalescence. Physical Review Fluids, 2020, 5(3): 033608.

Bhatnagar, P. L., Gross, E. P., Krook, M. A model for collision processes in gases. I. Small amplitude processes in charged and neutral one-component systems. Physical Review, 1954, 94(3): 511-525.

Burton, J. C., Taborek, P. Role of dimensionality and axisymmetry in fluid pinch-off and coalescence. Physical Review Letters, 2007, 98(22): 224502.

Burton, J. C., Huisman, F. M., Alison, P., et al. Experimental and numerical investigation of the equilibrium geometry of liquid lenses. Langmuir, 2010, 26(19): 15316-15324.

Cappelli, S., Xie, Q., Harting, J., et al. Dynamic wetting: status

and prospective of single particle based experiments and simulations. New Biotechnology, 2015, 32(5): 420-432.

Chen, H., Chen, S., Matthaeus, W. H. Recovery of the Navier-Stokes equations using a lattice-gas Boltzmann method. Physical Review A, 1992, 45(8): R5339-R5342.

Chen, L., Kang, Q., Mu, Y., et al. A critical review of the pseudopotential multiphase lattice boltzmann model: Methods and applications. International Journal of Heat and Mass Transfer, 2014, 76: 210-236.

Duchemin, L., Eggers, J., Josserand, C. Inviscid coalescence of drops. Journal of Fluid Mechanics, 2003, 487: 167-178.

Eddi, A., Winkels, K. G., Snoeijer, J. H. Influence of droplet geometry on the coalescence of low viscosity drops. Physical Review Letters, 2013, 111(14): 144502.

Eggers, J. Fontelos, M. A. Singularities: Formation, Structure, and Propagation. Cambridge, Cambridge University Press, 2015.

Eggers, J., Lister, J. R., Stone, H. A. Coalescence of liquid drops. Journal of Fluid Mechanics, 1999, 401: 293-310.

Eggers, J., Sprittles, J. E., Snoeijer, J. H. Coalescence dynamics. Annual Review of Fluid Mechanics, 2025, 57: 61-87.

Erneux, T., Davis, S. H. Nonlinear rupture of free films. Physics of Fluids, 1993, 5(5): 1117-1122.

Eslamian, M., Soltani-Kordshuli, F. Development of multiple-droplet drop-casting method for the fabrication of coatings and thin solid films. Journal of Coatings Technology and Research, 2018, 15: 271-280.

Goff, H. D. Instability and partial coalescence in whippable dairy emulsions. Journal of Dairy Science, 1997, 80(10): 2620-2630.

Gross, M., Steinbach, I., Raabe, D., et al. Viscous coalescence of droplets: A lattice Boltzmann study. Physics of Fluids, 2013, 25(5): 052101.

Hack, M. A., Tewes, W., Xie, Q., et al. Self-similar liquid lens coalescence. Physical Review Letters, 2020, 124(19): 194502.

Hernández-Sánchez, J. F., Lubbers, L. A., Eddi, A., et al. Symmetric and asymmetric coalescence of drops on a substrate. Physical Review Letters, 2012, 109(18): 184502.

Hessling, D. Simulation of drying suspensions on porous substrates. Eindhoven, Eindhoven University of Technology, 2017.

Hopper, R. W. Coalescence of two equal cylinders: Exact results for creeping viscous plane flow driven by capillarity. Journal of the American Ceramic Society, 1984, 67(12): C-262-C-264.

Hopper, R. W. Plane Stokes flow driven by capillarity on a free surface. Journal of Fluid Mechanics, 1990, 213: 349.

Kaneelil, P. R., Pahlavan, A. A., Xue, N., et al. Three-dimensional self-similarity of coalescing viscous drops in the thin-film regime. Physical Review Letters, 2022, 129(14): 144501.

Krüger, T., Kusumaatmaja, H., Kuzmin, A., et al. The lattice Boltzmann method: Principles and Practice. Cham, Switzerland, Springer Cham, 2017.

Kumar, S., Narsimhan, G., Ramkrishna, D. Coalescence in creaming emulsions. existence of a pure coalescence zone. Industrial & Engineering Chemistry Research, 1996, 35(9): 3155-3162.

Lee, M. W., Kang, D. K., Yoon, S. S., et al. Coalescence of two drops on partially wettable substrates. Langmuir, 2012, 28(8): 3791-3798.

Lim, S. J., Choi, M. C., Weon, B. M., et al. Lattice Boltzmann simulations for water coalescence. Applied Physics Letters, 2017, 111(10): 101602.

Liu, H., Kang, Q., Leonardi, C. R., et al. Multiphase lattice Boltzmann simulations for porous media applications: A review. Computational Geosciences, 2016, 20: 777-805.

Low, T. B., List, R. Collision, coalescence and breakup of raindrops. Part I: Experimentally established coalescence efficiencies and fragment size distributions in breakup. Journal of the Atmospheric Sciences, 1982, 39(7): 1591-1606.

Narhe, R. D., Beysens, D. A., Pomeau, Y. Dynamics drying in the early-stage coalescence of droplets sitting on a plate. Europhysics Letters, 2008, 81(4): 46002.

Padhan, N. B., Pandit, R. Unveiling the spatiotemporal evolution of liquid-lens coalescence: Self-similarity, vortex quadrupoles, and turbulence in a three-phase fluid system. Physics of Fluids, 2023, 35(11): 112105.

Paulsen, J. D., Burton, J. C., Nagel, S. R. Viscous to inertial crossover in liquid drop coalescence. Physical Review Letters, 2011, 106(11): 114501.

Paulsen, J. D., Burton, J. C., Nagel, S. R., et al. The inexorable resistance of inertia determines the initial regime of drop coalescence. Proceedings of the National Academy of Sciences of the United States of America, 2012, 109(18): 6857-6861.

Paulsen, J. D. Approach and coalescence of liquid drops in air. Physical Review E, 2013, 88(6): 063010.

Perazzo, A., Tomaiuolo, G., Preziosi, V., et al. Emulsions in porous media: from single droplet behavior to applications for oil recovery. Advances in Colloid and Interface Science, 2018, 256: 305-325.

Qian, Y. H., D'Humières, D., Lallemand, P. Lattice BGK models for Navier-Stokes equation. Europhysics Letters, 1992, 17(6): 479-484.

Ravazzoli, P. D., González, A. G., Diez, J. A., et al. Buoyancy and capillary effects on floating liquid lenses. Physical Review Fluids, 2020, 5(7): 073604.

Ristenpart, W. D., McCalla, P. M., Roy, R. V., et al. Coalescence of spreading droplets on a wettable substrate. Physical Review Letters, 2006, 97(6): 064501.

Scheel, T., Xie, Q., Sega, M., et al. Viscous to inertial coalescence of liquid lenses: A lattice Boltzmann investigation. Physical Review Fluids, 2023, 8(7): 074201.

Scheid, B., van Nierop, E. A., Stone, H. A. Thermocapillary-assisted pulling of contact-free liquid films. Physics of Fluids, 2012, 24(3): 032107.

Shan, X., Chen, H. Lattice Boltzmann model for simulating flows with multiple phases and components. Physical Review E, 1993, 47(3): 1815.

Shan, X., Chen, H. Simulation of nonideal gases and liquid-gas phase transitions by the lattice Boltzmann equation.

Physical Review E, 1994, 49(4): 2941.

Steinberger, M., Xie, Q., Ronsin, O. J. J., et al. Challenges and opportunities in upscaling inkjet-printing of OPV. Flexible and Printed Electronics, 2024, 9(4): 043001.

Succi, S. The Lattice Boltzmann Equation: For Fluid Dynamics and Beyond. Oxford, UK, Oxford University Press, 2001.

Thoroddsen, S. T., Qian, B., Etoh, T. G., et al. The initial coalescence of miscible drops. Physics of Fluids, 2007, 19(7): 072110.

Vinodh, R., Palanivel, T., Kalanur, S. S., et al. Recent advancements in catalyst coated membranes for water electrolysis: A critical review. Energy Advances, 2024, 3(6): 1144-1166.

Wijshoff, H. Drop dynamics in the inkjet printing process. Current Opinion in Colloid & Interface Science, 2018, 36: 20-27.

Xia, X., He, C., Zhang, P. Universality in the viscous-to-inertial coalescence of liquid droplets. Proceedings of the National Academy of Sciences of the United States of America, 2019, 116(47): 23467-23472.

Xie, Q., Du, T., Brabec, C. J., et al. Effect of particle and substrate wettability on evaporation-driven assembly of colloidal monolayers. Langmuir, 2025, 41(23): 14995-15003.

Yuan, X., Liang, H., Chai, Z., et al. Phase-field-based lattice Boltzmann model for immiscible incompressible *N*-phase flows. Physical Review E, 2020, 101(6): 063310.

Zhao Y., Fan, L.-S. Multirelaxation-time interaction-potential-based lattice boltzmann model for two-phase flow. Physical Review E, 2010, 82(4): 046708.

Zheng, L., Zheng, S. Phase-field-theory-based lattice Boltzmann equation method for *N* immiscible incompressible fluids. Physical Review E, 2019, 99(6): 063310.